Doping-mediated stabilization of copper vacancies to promote thermoelectric properties of Cu2−xS

Yu Zhang,[a]† Congcong Xing,[a]† Yu Liu,*[b] Maria Chiara Spadaro,[c] Xiang Wang,[a] Mengyao Li,[a] Ke Xiao,[a] Ting Zhang,[c] Pablo Guardia,[a] Ahmad Ostovari Moghaddam,[d] Jordi Arbiol,[c,e] Maria Ibáñez,[b] Andreu Cabot*[a,e]

[a] Catalonia Energy Research Institute—IREC, Sant Adria de Besos, 08930 Barcelona, Spain

[b] Institute of Science and Technology Austria, Am Campus 1, 3400 Klosterneuburg, Austria

[c] Catalan Institute of Nanoscience and Nanotechnology (ICN2), Campus UAB, Bellaterra, 08193 Barcelona, Spain

[d] South Ural State University, 76, Lenin Ave., Chelyabinsk 454080, Russia

[e] ICREA Pg. Lluis Companys, 08010 Barcelona, Spain

† These authors contributed equally to this work.

*Corresponding author: E-mail: yu.liu@ist.ac.at; acabot@irec.cat

Abstract: Copper chalcogenides are outstanding thermoelectric materials for applications in the medium-high temperature range. Among different chalcogenides, $Cu_{2-x}S$ provides advantages in terms of low cost and element abundance, but $Cu_{2-x}Se$ is characterized by higher thermoelectric figures of merit. In the present work, we investigate the effect of different dopants to enhance thermal stability and performance of $Cu_{2-x}S$. Among the tested options, Pb-doped $Cu_{2-x}S$ show the highest improvement in stability against sulfur volatilization at temperatures up to 880 K. Additionally, Pb incorporation allows tuning charge carrier concentration, which enables a significant improvement of the power factor. We demonstrate here that the introduction of an optimal additive amount of just 0.3% results in a threefold increase of the power factor in the middle-temperature range (500-800 K) and a dimensionless thermoelectric figure of merit above 2 at 880 K.

Keywords: copper sulfide, stabilization, copper vacancies, thermoelectric, nanocrystals

1. Introduction

Thermoelectric (TE) devices allow the solid-state conversion between heat and electricity.[1-5] Their efficiency is largely determined by a material figure of merit, $Z=\sigma S^2\kappa^{-1}$, generally expressed in a dimensionless form, ZT, where σ, S, κ and T stand for electrical conductivity, Seebeck coefficient, thermal conductivity, and absolute temperature, respectively.[1, 6-10] Despite the countless potential applications of thermoelectrics, both to harvest ubiquitous heat and to control temperature, the real implementation of TE devices has been limited to a few niche markets. The main limitations for the widespread use of thermoelectricity have been the high cost of the employed TE materials, usually based on scarce and expensive tellurium, and the limited energy conversion efficiency of TE devices, which overall result in systems that lack cost-effectiveness in most potential markets.

Copper chalcogenides, and particularly copper sulfides, are one of the oldest known TE materials and one of the most appealing due to the abundance and low cost of its constituent elements.[11-13] However, it was not until recently that its huge potential in the middle-high temperature range was revealed,[10, 14-18] with reports demonstrating ZT values up to 1.9 for $Cu_{2-x}S$[19] and well above 2 for $Cu_{2-x}Se$.[20]

Copper chalcogenides are characterized by a large versatility in compositions and crystal phases, consequence of the low size and electronegativity differences between copper and chalcogens, the fact that the formal chalcogen oxidation state is not necessarily two and the chalcogen ability to catenate.[21] A related additional characteristic of copper chalcogenides is their tolerance for a large range and density of non-stoichiometry and anti-site defects. This high defect concentration results in singular and highly tunable properties, including charge and heat transport, optoelectronic, optic and plasmonic.[21]

Despite its chemical simplicity, binary copper chalcogenides show a complex electronic structures and phase diagrams with numerous phases and stoichiometries.[21-26] The most

common $Cu_{2-x}S$ phases at ambient temperature are monoclinic low-chalcocite (Cu_2S), monoclinic djurleite ($Cu_{1.93-1.97}S$), triclinic roxybyite ($Cu_{1.81}S$), cubic digenite ($Cu_{1.8}S$), orthorhombic anilite ($Cu_{1.75}S$), and hexagonal covellite (CuS). All these crystallographic structures are based upon approximately hexagonal (djurlite, chalcocite, roxbyite and covellite) or cubic (anilite and digenite) close-packing of the sulfur atoms, with Cu atoms occupying various interstitial sites.[25, 27] When increasing temperature, copper ions become highly disordered, adopting a statistical distribution on different sites, which allows a higher crystallography symmetry defined by the sulfur framework:[28-32] Monoclinic low-chalcocite transforms into hexagonal high chalcocite at around 376 K, and into cubic chalcocite at about 709 K.[24, 27, 33, 34] At 346 K, cubic digenite undergoes a phase transition into a higher symmetry cubic phase known as high digenite that coincides with the cubic chalcocite phase.[32, 35, 36] Monoclinic djurlite transforms into a combination of hexagonal chalcocite and cubic high digenite at 363 K, and to pure cubic phase at around 700 K.[37] Anilite is also stable only to 345 K and transforms into high digenite.[32, 38]

The high copper disorder at moderate and high temperature gives rise to a virtually fluid-like ionic mobility and very low thermal conductivities. As a drawback, this Cu mobility gives rise to copper migration instabilities. In operating TE devices, these instabilities can be overcome by proper encapsulation, by limiting the working current at high temperature, and/or by introducing electron-conducting but ion-blocking layers.[39]

At ambient conditions, stoichiometric Cu_2S forms copper vacancies through surface oxidation, degrading into copper-deficient $Cu_{2-x}S$ phases, mainly dijurleite:[12, 40, 41] $Cu_2S \xrightarrow{O\downarrow} Cu_{1.96}S + Cu_2O$. This copper deficiency is not compensated by a change of the copper oxidation state, which stays close to Cu^+ regardless of the crystal structure and stoichiometry, but results in p-type compounds containing large charge carrier concentrations, up to 10^{21} cm^{-3}. On the other hand, when increasing temperature within a sulfur-free

atmosphere, CuS and $Cu_{2-x}S$ are unstable towards sulfur loss, evolving toward Cu-richer phases:[42-45] $CuS \xrightarrow{S\uparrow} Cu_{1.8}S \xrightarrow{S\uparrow} Cu_{1.96}S \xrightarrow{S\uparrow} Cu_2S$.

Extrinsic cation and anionic doping have been explored to promote $Cu_{2-x}S$ TE properties, both in terms of improving stability and performance. Table S1 lists previous attempts to improve $Cu_{2-x}S$ by incorporating foreign ions or secondary phases and the effects reported. In most cases, doping results in a decrease of the thermal conductivity and the charge carrier concentration, which has associated an increase of the Seebeck coefficient, but a concominant diminution of the electrical conductivity. This strategy has allowed obtaining ZT values up to 1.8 at 973 K by doping $Cu_{1.8}S$ with I.[46]

In the present study, we analyze the effect that different dopants have on the $Cu_{2-x}S$ stoichiometry and crystal phase, as main characteristics determining the material performance. After identifying Pb as the element having a major influence, we analyze the transport properties of materials doped with different amounts of this element. Results are correlated with crystallographic modifications obtained from high resolution transmission electron microscopy (HRTEM) and structural phase transitions observed by in-situ high-temperature x-ray diffraction (XRD) measurement up to 823 K.

2. Materials and methods

Chemicals and solvents: Copper (I) chloride (CuCl, ≥99%), sulfur powder (S, 99.998%, trace metals basis), 1-octadecene (ODE, technical grade 90%), lead oxide (PbO, 99.9%), indium(III) acetate (99.99% trace metals basis), tin (II) acetate, cadmium oxide (CdO, ≥99.99% trace metals basis) and zinc acetate (99.99% trace metals basis) were purchased from Sigma Aldrich. Oleylamine (OAm, C18 content approximately 80-90%,) was purchased from Fisher. Analytical grade ethanol and chloroform were obtained from various sources. All

chemicals were used as received, without further purification. All syntheses were carried out using standard vacuum/argon Schlenk lines.

S-OAm solution: To prepare S-OAm solution, 0.352 g S powder (11 mmol) was mixed with 7 mL OAm in a three-neck flask. The mixture was heated to 80 ºC for 30 min under vacuum to completely dissolve S in an oxygen free atmosphere.

$Cu_{2-x}S$ nanoparticles: In a typical synthesis, 20 mmol of CuCl was mixed with 35 ml of OAm and 15 mL ODE in a 100 mL three-neck flask. The mixture was degassed under vacuum for 20 min at room temperature and then heated to 100 ºC for 30 min under vacuum in order to obtain a clear solution and remove low boiling point impurities. Then the temperature was increased to 215 ºC under Ar. At this point, 7 mL of previously prepared S-OAm was injected into solution, which immediately changed color to dark brown. Upon injection, the temperature of the reaction mixture dropped to ~207 ºC. Temperature was allowed to recover to 215 ºC and maintained at this point for 20 min. Afterwards, the colloidal solution was rapidly cooled to room temperature with a water bath with approximate rate of ~80 ºC/min. Finally, 20 mL of chloroform were added to the crude solution and the product was precipitated by centrifugation at 8200 rpm for 5 min. Then it was redispersed in chloroform and precipitated one more time by centrifugation in the presence of ethanol. Finally, $Cu_{2-x}S$ nanoparticles were dried under vacuum and kept in an Ar-filled glovebox until their posterior use.

$Cu_{2-x}S$:M (M= In, Cd, Zn, Sn, Pb) nanoparticles: In a typical synthesis of $Cu_{2-x}S$:M colloidal nanoparticles, 20 mmol of CuCl and 0.09 mmol (correspond to 0.3%), 0.27 mmol (correspond to 0.9%), 0.54 mmol (correspond to 1.8%) and 1.5 mmol (correspond to 5%) of M precursor (indium acetate, cadmium oxide, zinc acetate, tin acetate, lead oxide) were weighted and mixed with 35 ml of OAm and 15 mL ODE in a 100 mL three-neck flask. The next steps were the same as for the production of $Cu_{2-x}S$ nanoparticles.

Nanomaterial consolidation into pellets: Dried $Cu_{2-x}S$ and $Cu_{2-x}S$:Pb nanopowders were introduced inside a tube furnace and annealed at 400 °C (heating rate = 10 ºC/min) for 1 h under an Ar flow. The annealed material was loaded into a graphite die and uniaxially hot-pressed into cylinders (Ø 8 mm× 2 mm) using a custom-made hot-press. This process was carried out within an argon-filled glove box. The hot press temperature was set at 400 ºC and pressure was increased up to 50 MPa for 300 s. Relative densities of the consolidated pellets were measured by the Archimedes' method.

Structural and chemical characterization: TEM studies were characterized by transmission electron microscopy (TEM, ZEISS LIBRA 120). HRTEM images and STEM studies were carried out on a FEI Tecnai F20 field emission gun microscope operated at 200 kV with a point-to-point resolution of 0.19 nm, which was equipped with high angle annular dark field (HAADF) and Gatan Quantum EELS detectors. 3D atomic models and HRTEM image simulations have been performed by using Rhodius[47, 48] and STEM_CELL[49, 50] software, respectively.

Elemental analysis was conducted using an Oxford EDX combined with the Zeiss Auriga SEM working at 20.0 kV. XRD characterization were carried out on a Bruker AXS D8 Advance X-ray diffractometer with Ni-filtered Cu-Kα radiation (λ= 1.5406 Å). For temperature-dependent XRD analysis, temperature was ramped at a rate of 20 K/min from 323 K to 823 K followed by subsequent cooling to 323 K and hold for 30 minutes at each measurement temperature. ICP characterization was conducted on a ICPE-9820 system and by laser-ablation inductively coupled plasma-optical emission spectroscopy (LA-ICP-OES). UV-Vis-NIR absorption spectra were performed on a LAMBDA 950 UV-Vis spectrophotometer (PerkinElmer).

Thermoelectric property measurement: Electrical resistivity and Seebeck coefficients were measured simultaneously in a LSR-3 LINSEIS system under helium atmosphere. Three measurements were performed at each temperature. Considering the system accuracy and the

measurement precision, an error of ca. 5% in the measurement of the electrical conductivity and Seebeck coefficients was estimated. The thermal conductivity was calculated according to $\kappa = \lambda C_p \rho$, where κ represents the total thermal conductivity, λ is the thermal diffusivity, C_p is heat capacity, and ρ is the measured density of each specimen. An LFA 1000 Laser Flash was applied to measure the thermal diffusivities (λ) of the samples with an estimated error of ca. 5%. C_{gi} is calculated using the experimental value,[51] and the density (ρ) values were measured by the Archimedes' method. Hall charge carrier concentrations (n_H) and mobilities (μ_H) at room temperature were measured with a on Van der Pauw and Hall Bar measurements (ezHEMS 1000, NanoMagnetics) using a magnetic field of 1 T. Values provided correspond to the average of 7 consecutive measurements, from which an error of ca. 10% was estimated.

3. Results and Discussion

Copper sulfide nanoparticles (NPs) were synthesized by injecting sulfur-oleylamine complex into a copper precursor solution at 215 °C (see the experimental section for details). The geometry of the produced NPs resembled triangular disks with 20 ± 4 nm lateral size and 10 ± 2 nm thickness (Fig.s 1a, S1). The NPs displayed a light yellow color when dispersed in hexane and a localized surface plasmon resonance in the near-infrared region with a maximum absorption at around 1100 nm (Fig. 1b). HRTEM showed the NPs to display a digenite $Cu_{1.8}S$ phase (space group FM-3M) with a=b=c=5.3870 Å (Fig. 1c). This crystallographic phase was confirmed by XRD analysis (JCPDS 01-072-1966, Fig. 1e).

Cubic digenite $Cu_{1.8}S$ NPs were annealed at temperatures in the range from 573 K to 773 K for 30 min in an argon atmosphere. This thermal process resulted in a significant loss of sulfur. According to XRD analysis (Fig. 1e), after annealing the NPs at 573 K a combination of digenite $Cu_{1.8}S$ and the metastable tetragonal $Cu_{1.96}S$ phase was obtained. When increasing the annealing temperature to 673 K, almost pure tetragonal $Cu_{1.96}S$ was produced. Further

increasing the annealing temperature to 773 K resulted in an additional sulfur loss to mostly monoclinic chalcocite Cu_2S.

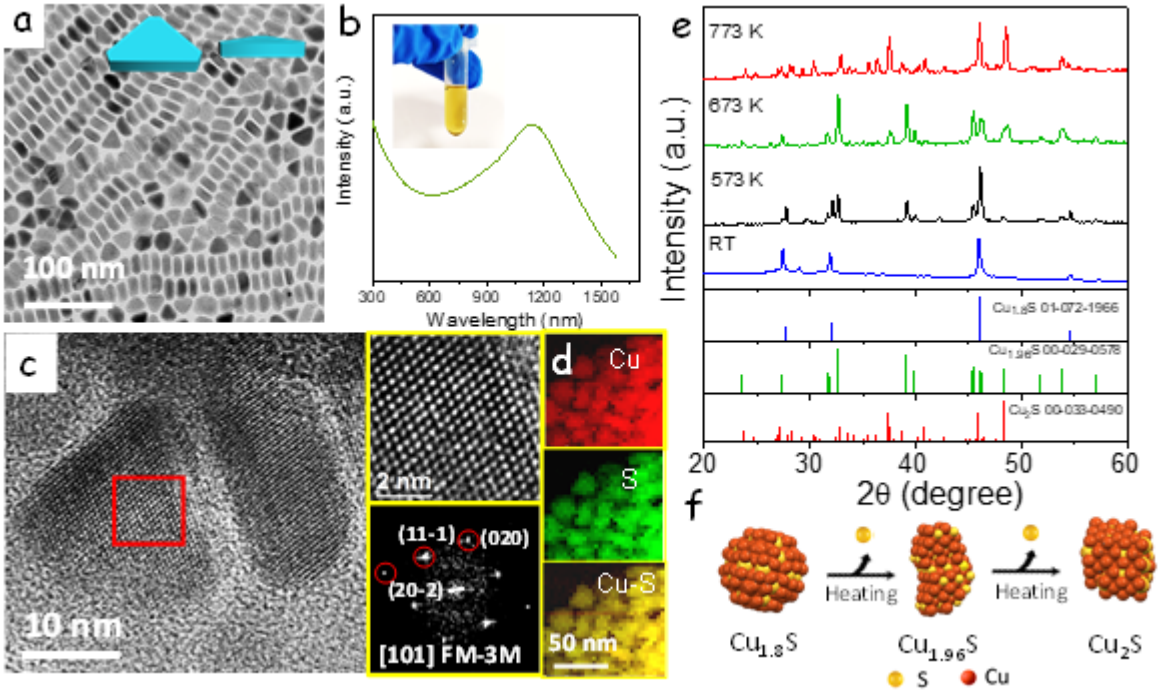

Fig. 1. (a) Representative TEM micrograph of $Cu_{2-x}S$ NPs. (b) UV-vis-NIR absorption spectrum of a colloidal suspension of $Cu_{2-x}S$ NPs. Inset shows the $Cu_{2-x}S$ colloid in hexane. (c) HRTEM micrograph of $Cu_{2-x}S$ NPs, magnified detail of the red squared region, and its corresponding power spectrum. (d) EELS chemical composition maps: individual Cu $L_{2,3}$-edges at 931 eV (red), S $L_{2,3}$-edges at 165 eV (green) and composite. (e) Powder XRD patterns of as-synthesized (RT) and annealed $Cu_{2-x}S$ NPs. The reference patterns for cubic digenite $Cu_{1.8}S$ (01-072-1966), tetragonal $Cu_{1.96}S$ (00-029-0578) and monoclinic chalcocite Cu_2S (00-033-0490) are also displayed. (f) Schematic illustration of sulfur loss upon heat treatment.

Different elements, In, Zn, Pb, Cd and Sn, were introduced as dopants within $Cu_{2-x}S$ at a 0.3% concentration (see details in the experimental section). SEM-EDX and ICP measurements showed that the final amount of additive within the produced particles was in most cases slightly lower than the nominal concentration of dopant added (Tables S2 and S3) XRD

analysis showed doped $Cu_{2-x}S$ NPs ($Cu_{2-x}S$:X, X=In, Cd, Zn, Sn, Pb) to also display the $Cu_{1.8}S$ phase (Fig. S2), in agreement with undoped $Cu_{2-x}S$. TEM characterization showed $Cu_{2-x}S$:In, $Cu_{2-x}S$:Zn, and $Cu_{2-x}S$:Cd NPs to have a quasi-spherical morphology, similar to that of undoped $Cu_{2-x}S$ NPs (Fig. 2a). On the other hand, $Cu_{2-x}S$:Sn and $Cu_{2-x}S$:Pb NPs displayed hexagonal/triangular disk morphologies and larger particle sizes, in the range 50-400 nm (Fig. 2a).

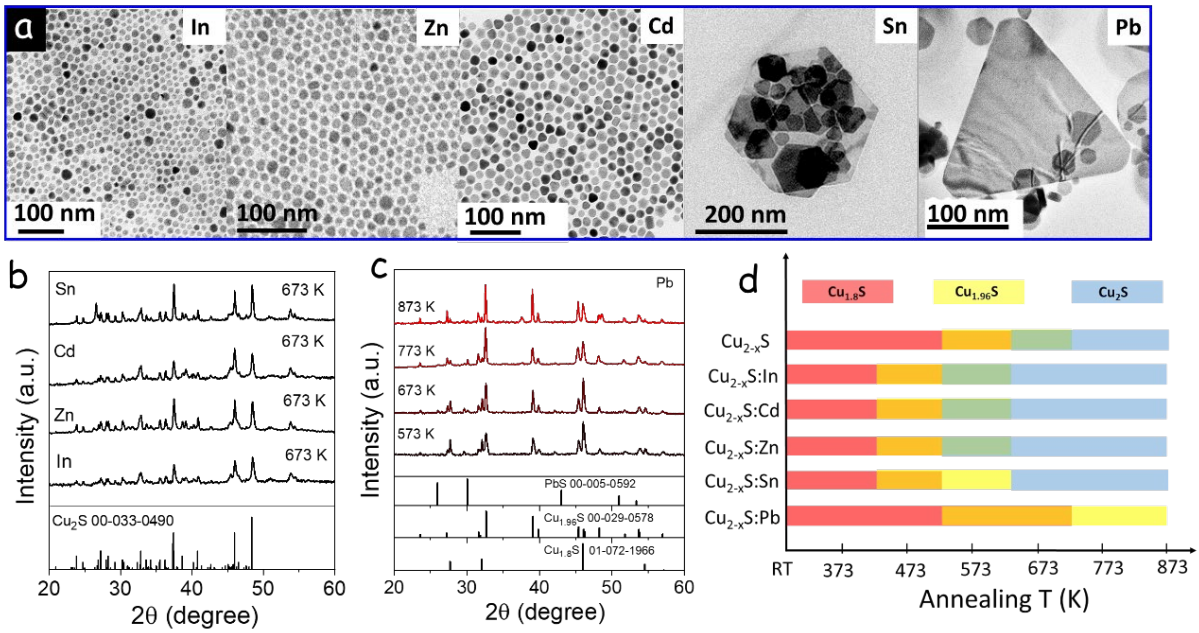

Fig. 2. (a) Representative TEM micrographs of $Cu_{2-x}S$:X (X=In, Zn, Sn, Cd, Pb) NPs. (b) XRD patterns of $Cu_{2-x}S$:X (X=In, Zn, Sn, Cd) nanopowders obtained after annealing the corresponding NPs at 673 K for 30 min and under Ar atmosphere. (c) XRD patterns of $Cu_{2-x}S$:Pb nanopowders obtained after annealing the corresponding NPs at 573K, 673 K, 773 K, and 873 K. (d) Scheme of the crystal phases obtained for undoped and doped $Cu_{2-x}S$ after annealing at different temperatures: Red = $Cu_{1.8}S$; Orange = $Cu_{1.8}S$ + $Cu_{1.96}S$; Yellow = $Cu_{1.96}S$; Green = $Cu_{1.96}S$ + Cu_2S; Blue = Cu_2S.

A significant sulfur loss was obtained upon annealing doped $Cu_{1.8}S$ NPs. Compared with undoped $Cu_{1.8}S$, the sulfur loss was slightly accentuated with the introduction of most dopants.

In this direction, $Cu_{1.8}S$:In, $Cu_{1.8}S$:Zn, $Cu_{1.8}S$:Cd, and $Cu_{1.8}S$:Sn NPs resulted in tetragonal $Cu_{1.96}S$ after thermal treatment at 573 K (Fig. S2), and already monoclinic Cu_2S after annealing at 673 K or higher temperatures (Fig. 2b,d). In contrast, $Cu_{1.8}S$:Pb NPs showed higher thermal stability against S volatilization, maintaining the tetragonal $Cu_{1.96}S$ phase even after annealing at 873 K (Fig. 2c,d).

Owing to the significant effect of Pb in blocking S loss and thus improving structural/compositional stability, we further studied a range of Pb concentrations, from 0.3% to 5%. XRD analysis of $Cu_{2-x}S$:Pb NPs with different amounts of Pb displayed the presence of no secondary phases at low Pb concentrations, but revealed the presence of PbS in samples containing 2% Pb and above, both before and after annealing (Fig. S3).

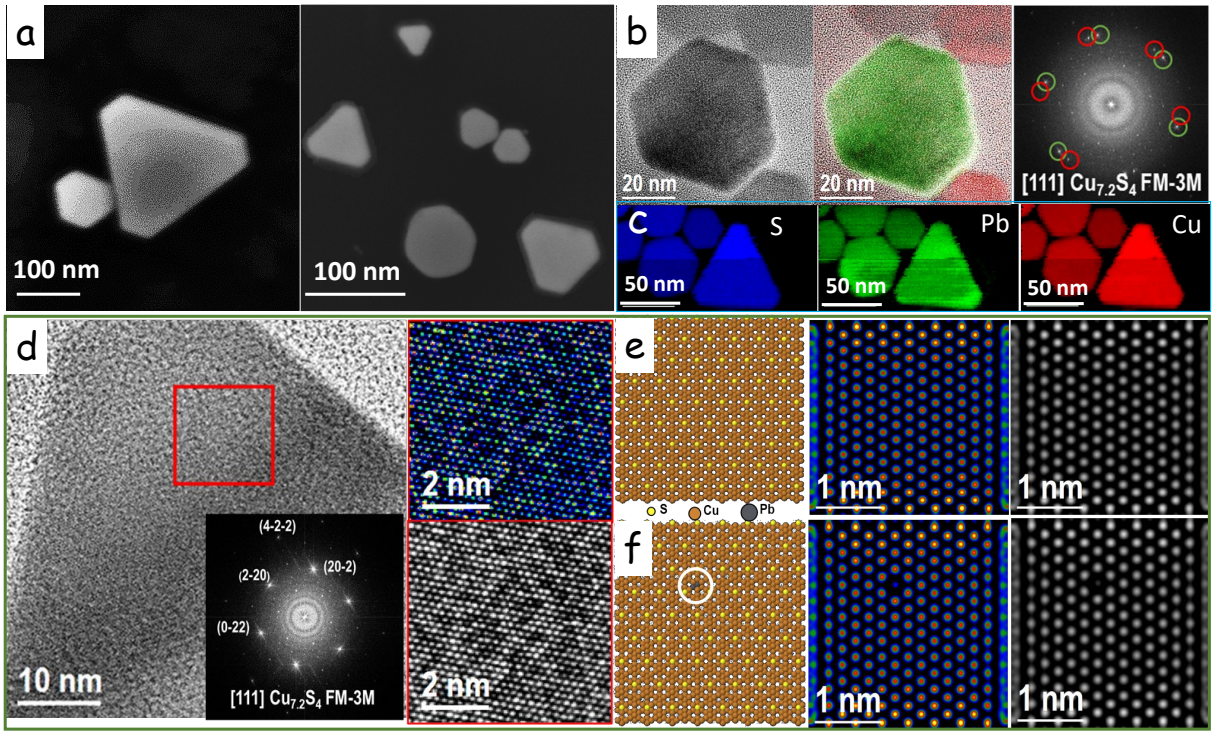

Fig. 3. Electron microscopy characterization of $Cu_{2-x}S$:Pb (0.9%) NPs. (a) Representative SEM micrographs. (b) HRTEM micrograph obtained at low magnification together with color frequency filtered map and the corresponding power spectrum. The color frequency filtered map highlighted the existence of different rotations of NPs (red and green), visualized along the zone axis [111]. (c) EELS chemical composition maps, individual Pb $N_{6,7}$-edge at 138 eV

(green), S $L_{2,3}$-edge at 165 eV (blue) and Cu $L_{2,3}$-edge at 931 eV (red). (d) HRTEM image and representative power spectrum obtained from the indicated red box area, on the right side we report the corresponding blow-up structure both in greyscale and temperature palette to highlight the peculiar image contrast at the atomic level caused by Pb substitution of Cu. (e), (f) 3D atomic models of (e) pure $Cu_{1.8}S$ (e) and $Cu_{1.8}S$:Pb (f), together with the HRTEM image simulation in grey and temperature palette. The white circle indicated the position where a Cu atom was substituted by a Pb atom.

SEM and HRTEM images of $Cu_{2-x}S$:Pb are displayed in Fig.s 3a and b, respectively. HRTEM micrographs and power spectrum analyses confirmed the as-produced $Cu_{2-x}S$:Pb NPs to display a $Cu_{1.8}S$ FM-3M structure. The presence of additional diffuse spots demonstrated the existence of a superstructure induced by Pb doping. The chemical composition maps, obtained by electron energy loss spectroscopy in scanning transmission electron microscopy mode (EELS-STEM), displayed a homogeneous distribution of Pb, Cu and S within each NPs, which indicated the incorporation of Pb within the $Cu_{1.8}S$ lattice (Fig. 3c). The Pb doping is also visible in the HRTEM micrographs displayed on the right side of Fig. 3d. In fact, Pb inclusion induced contrast differences in the HRTEM image, with brighter and darker areas as highlighted in the temperature palette (top right side of Fig. 3d) and greyscale (bottom right side of Fig. 3d). To verify the local doping variation from HRTEM image contrast evaluation, we created a 3D atomic model to observe the effect of locally substituting Cu atoms with Pb in the crystal structure (Fig. 3e-f): in Fig. 3e we report the undoped model while in Fig. 3f we report the model where Cu atoms were substituted by Pb atoms (in the region highlighted with the white circle area). By performing HRTEM image simulation from the above described 3D atomic models, we confirmed that the presence of heavier Pb atoms generate dark contrast spots in both temperature palette and greyscale images in Fig. 3f. We can immediately

perceive this difference when comparing the simulated images in Fig. 3f (doped case) with the ones in Fig. 3e (undoped case). This result further confirmed the presence of Pb within the $Cu_{1.8}S$ lattice substituting Cu atoms and creating a superstructure that overlapped to digenite $Cu_{1.8}S$. This result was consistent with the presence of additional spots in the power spectrum, especially along the [112] family planes, indicating a high degree of order for the Pb substitutions.

Additional detailed studies were also performed for the $Cu_{2-x}S$:In sample, obtaining similar results (Fig. S4), which demonstrates the high capacity of $Cu_{2-x}S$ to accommodate foreign atoms in its lattice and the high ordering degree for the substitutional atoms obtained with the synthesis process here presented.

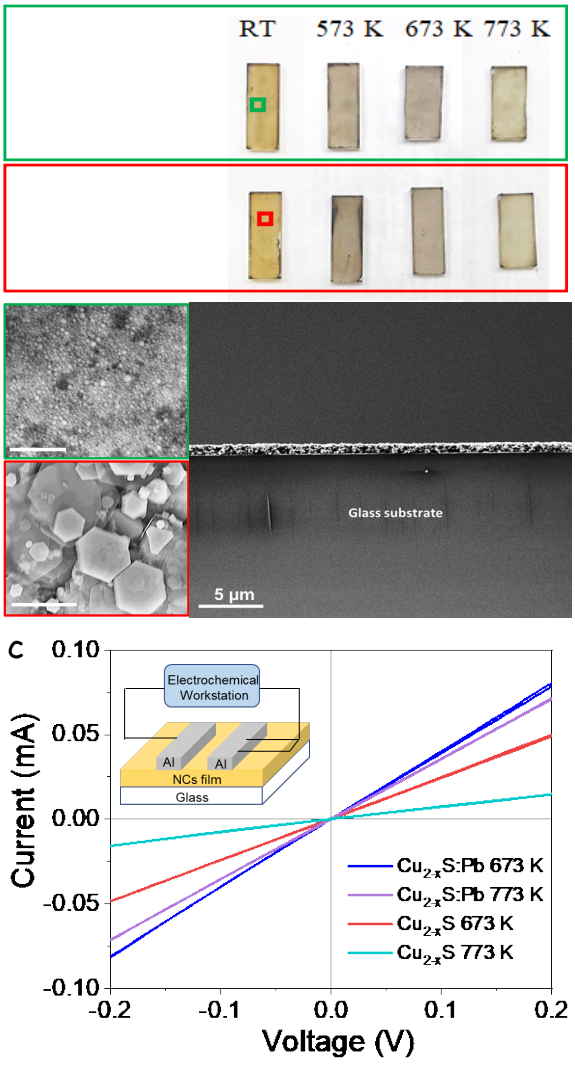

Fig. 4. (a) Optical images of $Cu_{2-x}S$ and $Cu_{2-x}S$:Pb NP films without annealing (RT) and annealed at 573, 673 and 773 K. (b) Top-view SEM images of a $Cu_{2-x}S$ (green-framed) and $Cu_{2-x}S$:Pb (red-framed) NP films and cross-section SEM image of the $Cu_{2-x}S$:Pb NP film. The same scale bar applies for the three displayed SEM images. (c) Current-voltage plots of $Cu_{2-x}S$ and $Cu_{2-x}S$:Pb (0.3%) films annealed at 673 and 773 K. The inset schematically shows the set-up used for electrical conductivity measurements.

A first assessment of the electrical conductivity of $Cu_{2-x}S$ and $Cu_{2-x}S$:Pb was obtained with the material deposited in the form of a thin film. As-produced $Cu_{2-x}S$ NPs were deposited by spin coating on top of a glass substrate using a 90 mg/mL colloidal dispersion in hexane. Fig. 4b displays cross-section and top-view SEM images of the $Cu_{2-x}S$:Pb (0.3%) film before annealing. The obtained films were annealed at a temperature in the range 573 -773 K. A color change from lighter to darker brown was observed when increasing the annealing temperature, as shown in the optical images of $Cu_{2-x}S$ and $Cu_{2-x}S$:Pb films before and after annealing (Fig. 4a). Al electrodes were deposited on top of the films to measure their i-v characteristics. We observed the room temperature electrical conductivity of $Cu_{2-x}S$ and $Cu_{2-x}S$:Pb to decrease with the film annealing temperature, which was associated with the loss of sulfur. This variation of the electrical conductivity with the annealing temperature was especially dramatic for bare $Cu_{2-x}S$, where the electrical conductivity decreased from 11.3 S/m for the film annealed at 673 K to 4.2 S/m for the film annealed at 773 K. Additionally, we also observed the electrical conductivity of $Cu_{2-x}S$:Pb to be significantly larger than that of bare $Cu_{2-x}S$: 21.7 S/m and 17.5 S/m for $Cu_{2-x}S$:Pb films annealed at 673 K and 773 K, respectively. This higher electrical conductivity was well correlated with the higher sulfur content of annealed $Cu_{2-x}S$:Pb when compared with $Cu_{2-x}S$.

$Cu_{2-x}S$ and $Cu_{2-x}S$:Pb NPs annealed at 673 K were hot-pressed at 673 K and 50 MPa for 300 s within an Ar-filled atmosphere (Fig. 5a). The produced $Cu_{2-x}S$ and $Cu_{2-x}S$:Pb pellets were characterized by 88% relative densities and an average crystal domain size of around 1 µm, as observed by cross-section SEM (Fig. 5b). XRD analysis showed the hot-pressed $Cu_{2-x}S$ sample to display a majoritarian $Cu_{1.96}S$ phase with a significant presence of chalcocite Cu_2S (Fig. 5c). On the other hand, $Cu_{2-x}S$:Pb pellets contained a combination of $Cu_{1.8}S$ and $Cu_{1.96}S$ phases (Fig. 5c). Besides, XRD patterns showed the presence of the PbS phase only on $Cu_{2-x}S$:Pb pellets containing 2% Pb or above (Fig. 5c).

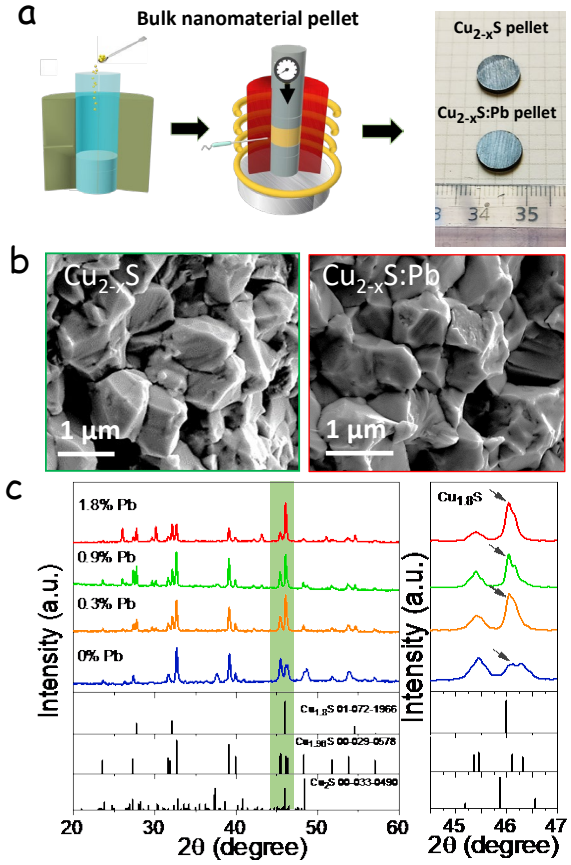

Fig. 5. (a) Scheme of the process used to produce $Cu_{2-x}S$ pellets by hot pressing the annealed NPs. (b) Cross-section SEM micrograph of $Cu_{2-x}S$ and $Cu_{2-x}S$:Pb (0.3%) pellets. (c) XRD pattern of $Cu_{2-x}S$ (blue) and $Cu_{2-x}S$:Pb pellets with different Pb concentrations: 0.3% (orange), 0.9% (green), and 1.8% (red). The standard diffraction pattern of monoclinic chalcocite Cu_2S

(JCPDS 00-033-0490), tetragonal $Cu_{1.96}S$ (JCPDS 00-029-0578) and digenite $Cu_{1.8}S$ (JCPDS 01-072-1966) are displayed as references.

The evolution of the crystal phase with temperature was analyzed using a high-temperature XRD chamber filled with argon (see the experimental section for details). Undoped $Cu_{2-x}S$ pellets displayed a phase transition from the combination of mainly tetragonal $Cu_{1.96}S$ and residual monoclinic Cu_2S observed at ambient temperature, to a combination of mainly hexagonal Cu_2S and additional rhombohedral $Cu_{1.8}S$ in the temperature range 373-423 K (Fig. 6). This combination of phases progressively transformed into cubic Cu_2S, which was identified as the unique phase at 823 K. On the other hand, the $Cu_{2-x}S$:Pb pellet displayed a phase transition from a combination of tetragonal $Cu_{1.96}S$ and cubic $Cu_{1.8}S$, to a mixture of cubic $Cu_{1.8}S$ and hexagonal Cu_2S at 423 K (Fig. 6). The hexagonal Cu_2S component decreased when increasing temperature, and already at 573 K only the cubic phase was obtained.

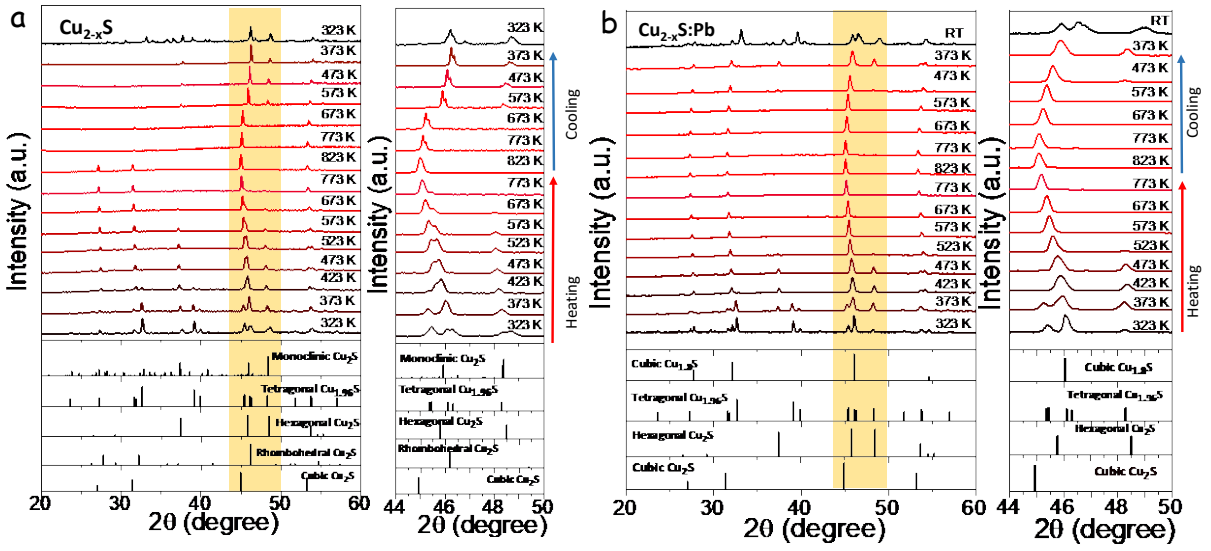

Fig. 6. High temperature XRD data from $Cu_{2-x}S$ (a) and $Cu_{2-x}S$:Pb (0.3%) pellets (b). From the bottom to the top pattern, the temperature was increased from ambient (RT) to 823 K and then decreased to 323 K. The standard diffraction pattern of monoclinic Cu_2S (JCPDS 00-033-0490), tetragonal $Cu_{1.96}S$ (JCPDS 00-029-0578), hexagonal Cu_2S (JCPDS 00-026-1116),

rhombohedral Cu_2S (JCPDS 00-047-1748), cubic Cu_2S (JCPDS 01-084-1770), and cubic $Cu_{1.8}S$ (JCPDS 01-072-1966) are included as a reference.

The electrical conductivity, Seebeck coefficient, thermal conductivity, and figure of merit of $Cu_{2-x}S$ and $Cu_{2-x}S$:Pb (0.3%) pellets stabilized at 880 K during 10 min are displayed in Fig. 7. The transport properties of $Cu_{2-x}S$:Pb pellets with different amounts of Pb are compared in Fig. S11. Because best TE performances were obtained with the material containing a 0.3% Pb, in the following we focus our discussion on this material. $Cu_{2-x}S$:Pb exhibited twofold higher electrical conductivities than pure $Cu_{2-x}S$. This increase of electrical conductivity with the Pb introduction was correlated with an increase of the charge carrier concentration, as evidenced by Hall measurements (Fig. S6). The higher charge carrier concentrations and electrical conductivities measured in the presence of Pb are in contrast with previous works reporting opposite results with the introduction of Pb.[52, 53] Actually, as noted in prevous works, a decrease of the hole concentration is expected if considering that Pb^{2+} ions replace Cu^{1+} ions or occupy copper vacancies within the $Cu_{2-x}S$ structure. Thus, the increase of the charge carrier concentration measured here cannot be directly explained by the presence of electronically active Pb^{2+} impurities, but it needs to be indirectly related with the effect that the Pb presence has on the $Cu_{2-x}S$ stoichiometry. In $Cu_{2-x}S$, the concentration of charge carriers (holes) is correlated with the density of copper vacancies.[54] With the annealing of the materials in an inert atmosphere, some sulfur is lost, which increases the Cu/S ratio and thus decreases the hole concentration. As shown above, the presence of Pb within the $Cu_{2-x}S$ lattice stabilizes a larger amount of sulfur, thus maintaining a larger density of copper vacancies and hence a higher charge carrier concentration. As shown in Fig. 5c, this effect directly depends on the introduced amount of Pb: the higher the Pb concentration, the larger the XRD peaks associated to the $Cu_{1.8}S$ phase, thus the lower the Cu/S ratio and consequently the hole concentration (Fig.s S5, S6).

The transport properties of $Cu_{2-x}S$:Pb were observed to be much more stable upon repetitive cycling than those of undoped $Cu_{2-x}S$. This is shown in Fig. S9 where 10 consecutive measurement cycles up to 880 K are displayed for each sample. The stability improvement with the incorporation of small amounts of Pb is also related to the stabilization of larger amounts of sulfur within the structure. It should be noticed that the annealing of $Cu_{2-x}S$ samples at relatively high temperatures, *ca*. 800 K, resulted in the appearance of a thin layer of copper(I) oxide on the pellet surface, which was not observed on $Cu_{2-x}S$:Pb (Fig. S7). The formation of surface cuprous oxide is generally ascribed to Cu-rich samples, i.e. Cu_2S, that loses Cu through oxidation in the surface when in contact with air.[12, 40, 41]

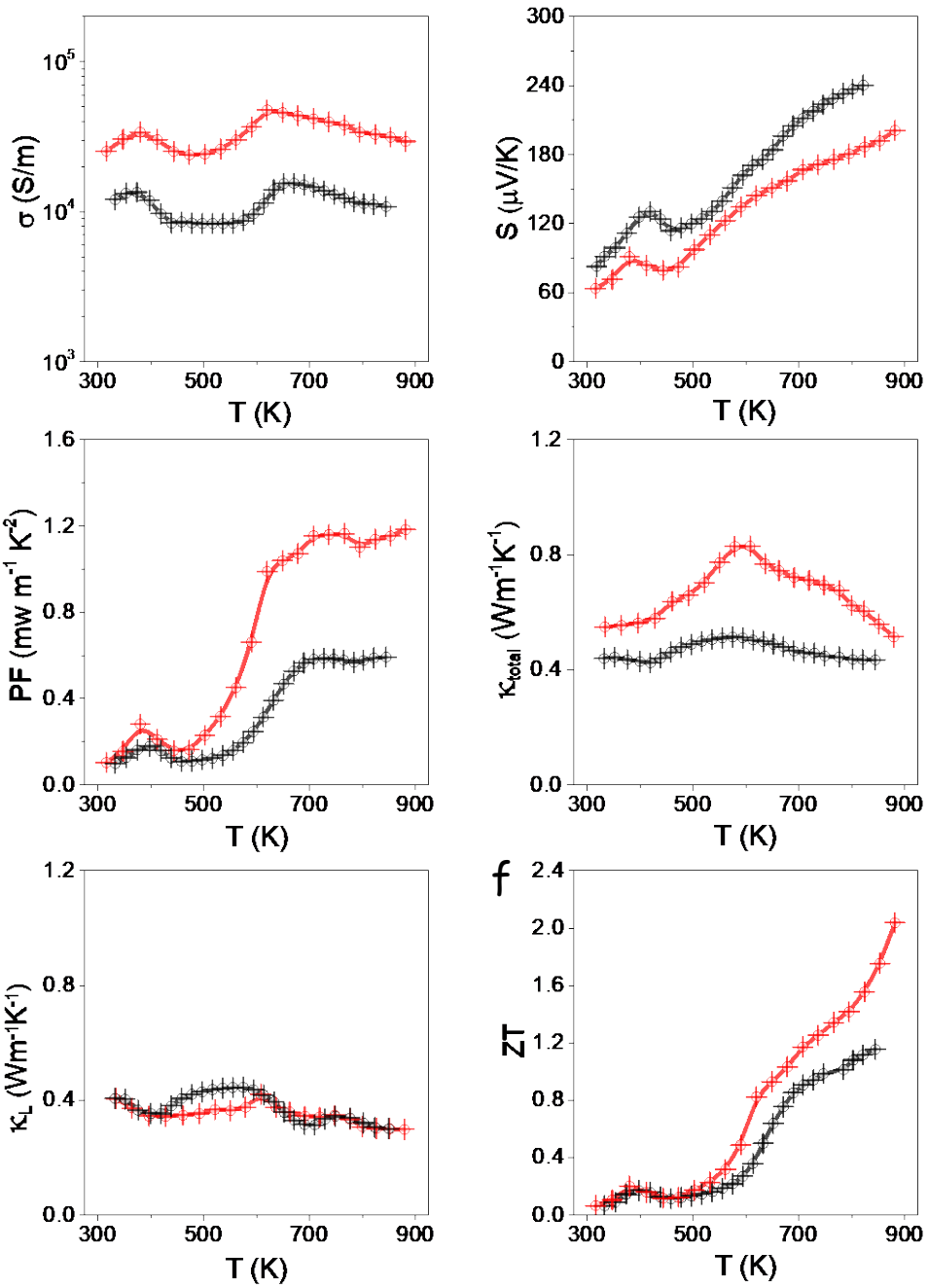

Fig. 7. Transport properties of $Cu_{2-x}S$ (black) and $Cu_{2-x}S$:Pb (0.3%, red). (a) Electrical conductivity, σ; (b) Seebeck coefficient, S; (c) Power factor, PF; (d) Total thermal conductivity, κ_{total}; (e) Lattice thermal conductivity, κ_L; (f) Figure of merit, ZT.

As expected, all samples exhibited positive Seebeck coefficients in the whole temperature range, consistent with their p-type character. Seebeck coefficients decreased with the amount of Pb introduced, consistently with the increase of the charge carrier concentration (Fig.s 7b,

S11b). S values monotonously increased with temperature except for a bump in the temperature range 350-450 K that matched well with the temperature range of the phase transitions observed in Fig. 6. Taking into account the measured σ and S values, the highest power factors ($PF=S^2\sigma$) were obtained for $Cu_{2-x}S$:Pb samples, reaching values up to 1.18 at 880 K (Fig.s 7c, S11c).

The total thermal conductivity κ_{total} of $Cu_{2-x}S$:Pb pellets was significantly larger than that of $Cu_{2-x}S$, which was related to the much higher electronic contribution, κ_e, of the former (Fig. 7d). Once subtracted the electronic contribution to the thermal conductivity, $Cu_{2-x}S$:Pb and $Cu_{2-x}S$ samples displayed similar lattice thermal conductivities (Fig. 7e). Thus, no decrease of the lattice thermal conductivity was obtained with the Pb incorporation, denoting a minor influence of the phonon scattering at Pb impurities, in contrast with previous reports.[52, 53] The discrepancy with previous reports could be ascribed to the low amount of Pb introduced here and the already low lattice thermal conductivity measured for our polycrystalline $Cu_{2-x}S$ pellets.

Overall $Cu_{2-x}S$:Pb pellets displayed significantly improved thermoelectric figures of merit ZT when compared with $Cu_{2-x}S$ and previously reported $Cu_{2-x}S$-based materials (Fig. 7f). Additionally, results obtained from $Cu_{2-x}S$:Pb showed good repeatability from sample to sample, as shown in fig. S10 where results from three different $Cu_{2-x}S$:Pb (0.3%) pellets obtained from different NP batches are displayed. At the highest tested temperature, 880 K, $Cu_{2-x}S$:Pb samples reached ZT = 2.03 (Fig. 7f), which is the highest TE figure of merit reported for a copper sulfide (Fig. S12, Table S4).

4. Conclusion

We investigated the effect of different dopants and annealing treatments on the crystal structure and stoichiometry of $Cu_{2-x}S$ nanoparticles and annealed nanopowders. Among the considered dopants, Pb displayed the largest effect. Pb substituted Cu atoms within the $Cu_{1.8}S$

lattice and created a superstructure that overlapped to digenite $Cu_{1.8}S$. This Pb-doped $Cu_{2-x}S$ showed a significant improvement in stability against sulfur volatilization at temperatures up to 880 K, which translated into a different evolution of the $Cu_{2-x}S$ crystal phases with temperature and major differences in the measured transport properties. $Cu_{2-x}S$:Pb films and pellets displayed much larger charge carrier concentrations and electrical conductivities than bare $Cu_{2-x}S$, which was associated with the effect that Pb had on the stabilization of higher amounts of S and thus of copper vacancies within the structure. At an optimal Pb concentration of just a 0.3% a dimensionless TE figure of merit, ZT = 2.03 at 880 K was obtained, which is the highest value obtained for $Cu_{2-x}S$.

Acknowledgements

This work was supported by the European Regional Development Funds and by the Spanish Ministerio de Economía y Competitividad through the project SEHTOP (ENE2016-77798-C4-3-R). MI acknowledges financial support from IST Austria. YL acknowledges funding from the European Union's Horizon 2020 research and innovation program under the Marie Sklodowska-Curie grant agreement No. 754411. YZ, CX, XW, KX and TZ thank the China Scholarship Council for the scholarship support. ICN2 acknowledges funding from Generalitat de Catalunya 2017 SGR 327 and the Spanish MINECO project ENE2017-85087-C3. ICN2 is supported by the Severo Ochoa program from the Spanish MINECO (grant no. SEV-2017-0706) and is funded by the CERCA program/Generalitat de Catalunya. Part of the present work has been performed in the framework of Universitat Autònoma de Barcelona Materials Science PhD program. M.C.S. has received funding from the European Union's Horizon 2020 research and innovation programme under the Marie Skłodowska-Curie grant agreement No. 754510 (PROBIST) and the Severo Ochoa programme. YZ and CX contributed equally to this work.

References

[1] S. Ortega, M. Ibáñez, Y. Liu, Y. Zhang, M.V. Kovalenko, D. Cadavid, A. Cabot, Chemical Society Reviews, 46 (2017) 3510-3528.

[2] A.I. Hochbaum, R. Chen, R.D. Delgado, W. Liang, E.C. Garnett, M. Najarian, A. Majumdar, P. Yang, Nature, 451 (2008) 163-167.

[3] F.J. DiSalvo, Science, 285 (1999) 703-706.

[4] L.A. Algharagholy, Q. Al-Galiby, H.A. Marhoon, H. Sadeghi, H.M. Abduljalil, C.J. Lambert, Nanotechnology, 26 (2015) 475401.

[5] L.-D. Zhao, S.-H. Lo, Y. Zhang, H. Sun, G. Tan, C. Uher, C. Wolverton, V.P. Dravid, M.G. Kanatzidis, Nature, 508 (2014) 373-377.

[6] G.J. Snyder, E.S. Toberer, Complex thermoelectric materials, Materials for sustainable energy: a collection of peer-reviewed research and review articles from Nature Publishing Group, World Scientific2011, pp. 101-110.

[7] M. Ibáñez, R. Hasler, A. Genç, Y. Liu, B. Kuster, M. Schuster, O. Dobrozhan, D. Cadavid, J. Arbiol, A. Cabot, Journal of the American Chemical Society, 141 (2019) 8025-8029.

[8] M. Ibánez, Z. Luo, A. Genc, L. Piveteau, S. Ortega, D. Cadavid, O. Dobrozhan, Y. Liu, M. Nachtegaal, M. Zebarjadi, Nature communications, 7 (2016) 1-7.

[9] Y. Pei, X. Shi, A. LaLonde, H. Wang, L. Chen, G.J. Snyder, Nature, 473 (2011) 66-69.

[10] H. Liu, X. Shi, F. Xu, L. Zhang, W. Zhang, L. Chen, Q. Li, C. Uher, T. Day, G.J. Snyder, Nature materials, 11 (2012) 422-425.

[11] G. Dennler, R. Chmielowski, S. Jacob, F. Capet, P. Roussel, S. Zastrow, K. Nielsch, I. Opahle, G.K. Madsen, Advanced Energy Materials, 4 (2014) 1301581.

[12] A.C. Becquerel, Annales de chimie et de physique, 35 (1827) 328.

[13] A.E. Becquerel, Annales de chimie et de physique. 48 (1866) 389.

[14] Z.-H. Ge, L.-D. Zhao, D. Wu, X. Liu, B.-P. Zhang, J.-F. Li, J. He, Materials Today, 19 (2016) 227-239.

[15] T.-R. Wei, Y. Qin, T. Deng, Q. Song, B. Jiang, R. Liu, P. Qiu, X. Shi, L. Chen, Science China Materials, 62 (2019) 8-24.

[16] K. Suekuni, T. Takabatake, Apl Materials, 4 (2016) 104503.

[17] Y. He, T. Day, T. Zhang, H. Liu, X. Shi, L. Chen, G.J. Snyder, Advanced Materials, 26 (2014) 3974-3978.

[18] W.D. Liu, L. Yang, Z.G. Chen, J. Zou, Advanced Materials, 32 (2020) 1905703.

[19] L. Zhao, X. Wang, F.Y. Fei, J. Wang, Z. Cheng, S. Dou, J. Wang, G.J. Snyder, Journal of Materials Chemistry A, 3 (2015) 9432-9437.

[20] A. Olvera, N. Moroz, P. Sahoo, P. Ren, T. Bailey, A. Page, C. Uher, P. Poudeu, Energy & Environmental Science, 10 (2017) 1668-1676.

[21] C. Coughlan, M. Ibanez, O. Dobrozhan, A. Singh, A. Cabot, K.M. Ryan, Chemical reviews, 117 (2017) 5865-6109.

[22] Y. Zhang, Y. Wang, L. Xi, R. Qiu, X. Shi, P. Zhang, W. Zhang, The Journal of chemical physics, 140 (2014) 074702.

[23] S. Djurle, X. An, Acta Chem. Scand, 12 (1958) 1415-1426.

[24] D. Chakrabarti, D. Laughlin, Bulletin of Alloy Phase Diagrams, 4 (1983) 254-271.

[25] R.J. Goble, The Canadian Mineralogist, 23 (1985) 61-76.

[26] P. Waldner, Journal of Phase Equilibria and Diffusion, 39 (2018) 810-819.

[27] P. Lukashev, W.R. Lambrecht, T. Kotani, M. van Schilfgaarde, Physical Review B, 76 (2007) 195202.

[28] J.B. Rivest, L.-K. Fong, P.K. Jain, M.F. Toney, A.P. Alivisatos, The Journal of Physical Chemistry Letters, 2 (2011) 2402-2406.

[29] W.R. Cook, Phase changes in Cu2S as a function of temperature, National Bureau of Standards1972.

[30] K. Okamoto, S. Kawai, Japanese Journal of Applied Physics, 12 (1973) 1130.

[31] M. Posfai, P.R. Buseck, American Mineralogist, 79 (1994) 308-315.

[32] G. Stapfer, P. Rouklove, L. Garvey, Jet Propulsion Lab., Pasadena, CA (USA)1977.

[33] J. Duan, C. Zhu, M. Guan, P. Lu, Y. He, Z. Fu, L. Zhang, F. Xu, X. Shi, L. Chen, Ceramics International, 44 (2018) 13076-13081.

[34] D.R. Brown, T. Day, K.A. Borup, S. Christensen, B.B. Iversen, G.J. Snyder, Apl Materials, 1 (2013) 052107.

[35] N. Morimoto, G. Kullerud, American Mineralogist: Journal of Earth and Planetary Materials, 48 (1963) 110-123.

[36] G. Will, E. Hinze, A.R.M. Abdelrahman, European Journal of Mineralogy, 14 (2002) 591-598.

[37] E.H. Roseboom, Economic Geology, 61 (1966) 641-672.

[38] N. Morimoto, K. Koto, Y. Shimazaki, American Mineralogist: Journal of Earth and Planetary Materials, 54 (1969) 1256-1268.

[39] P. Qiu, M.T. Agne, Y. Liu, Y. Zhu, H. Chen, T. Mao, J. Yang, W. Zhang, S.M. Haile, W.G. Zeier, Nature communications, 9 (2018) 1-8.

[40] J.M. Luther, P.K. Jain, T. Ewers, A.P. Alivisatos, Nature materials, 10 (2011) 361-366.

[41] A. Putnis, Philosophical Magazine, 34 (1976) 1083-1086.

[42] Z.-H. Ge, B.-P. Zhang, Y.-X. Chen, Z.-X. Yu, Y. Liu, J.-F. Li, Chemical Communications, 47 (2011) 12697-12699.

[43] M. Nair, L. Guerrero, P. Nair, Semiconductor Science and Technology, 13 (1998) 1164.

[44] L. Liu, C. Liu, W. Fu, L. Deng, H. Zhong, ChemPhysChem, 17 (2016) 771-776.

[45] L. Liu, B. Zhou, L. Deng, W. Fu, J. Zhang, M. Wu, W. Zhang, B. Zou, H. Zhong, The Journal of Physical Chemistry C, 118 (2014) 26964-26972.

[46] S. Zhao, H. Chen, X. Zhao, J. Luo, Z. Tang, G. Zeng, K. Yang, Z. Wei, W. Wen, X. Chen, Materials Today Physics, 15 (2020) 100271.

[47] J. Arbiol, A. Cirera, F. Peiró, A. Cornet, J. Morante, J. Delgado, J. Calvino, Applied physics letters, 80 (2002) 329-331.

[48] S. Bernal, F. Botana, J. Calvino, C. Lopez-Cartes, J. Perez-Omil, J. Rodrıguez-Izquierdo, Ultramicroscopy, 72 (1998) 135-164.

[49] V. Grillo, E. Rotunno, Ultramicroscopy, 125 (2013) 97-111.

[50] M.C. Spadaro, S. D'Addato, P. Luches, S. Valeri, V. Grillo, E. Rotunno, M.A. Roldan, S.J. Pennycook, A.M. Ferretti, E. Capetti, Nanotechnology, 26 (2015) 405704.

[51] W.-D. Liu, X.-L. Shi, H. Gao, R. Moshwan, S.-D. Xu, Y. Wang, L. Yang, Z.-G. Chen, J. Zou, Journal of Materials Chemistry C, 7 (2019) 5366-5373.

[52] Y. Zhou, Z.-H. Ge, G.-Y. Gan, P. Song, J. Feng, Solid State Sciences, 95 (2019) 105953.

[53] Y.-X. Zhang, Z. Ma, Z.-H. Ge, P. Qin, F. Zheng, J. Feng, Journal of Alloys and Compounds, 764 (2018) 738-744.

[54] P. Qiu, Y. Zhu, Y. Qin, X. Shi, L. Chen, APL Materials, 4 (2016) 104805.